Anderson, M. E., D. G. Schneider, J. L. Buckles, D. J. Bodine, A. E. Reinhart, M. A. Satrio, and T. Maruyama, 2022: Terrain effects on the 13 April 2018 Mountainburg, Arkansas EF2 tornado. *J. Operational Meteor.*, **10** (2), 18-29, doi: https://doi.org/10.15191/nwajom.2022.1002.

Journal of Operational Meteorology
Article

Terrain Effects on the 13 April 2018 Mountainburg, Arkansas EF2 Tornado

MATTHEW E. ANDERSON
NOAA/National Weather Service, Huntsville, AL

DOUG G. SCHNEIDER and JEREMY L. BUCKLES
NOAA/National Weather Service, Morristown, TN

DAVID J. BODINE
Advanced Radar Research Center and School of Meteorology, University of Oklahoma, Norman, Oklahoma

ANTHONY E. REINHART
NOAA/OAR/National Severe Storms Laboratory, Norman, Oklahoma

MARTIN A. SATRIO
School of Meteorology, University of Oklahoma, Norman, Oklahoma

TAKASHI MARUYAMA
Disaster Prevention Research Institute, Kyoto University, Kyoto, Japan

(Manuscript received 24 February 2021; review completed 11 February 2022)

ABSTRACT

Storm-scale interactions with rough terrain are complex. Terrain has been theorized to impact the strength of low-level mesocyclones. Surface roughness and modifications of the surrounding environment also may impact tornadogenesis or tornado intensity. The Mountainburg, Arkansas EF2 tornado on 13 April 2018 traveled along a path with minor variations in intensity and elevation throughout most of the nearly 19-km (11.8 mi) damage path as the storm moved along a river valley. A detailed damage survey showed that the tornado then made an abrupt ascent of more than 200 m (656 ft) in the last 2 km (1.2 mi) before dissipating. By examining model soundings and conducting a detailed terrain analysis, this study examines what role terrain may have had in channeling the momentum surge and enhancing the low-level vorticity to influence tornadogenesis. Other storm-scale factors are investigated to determine their potential impact on the demise of the tornado. The differential reflectivity column is studied to determine if the updraft was weakening. The relative position of the tornado and mesocyclone also are examined as the tornado ascended the terrain and dissipated to determine whether the change in elevation impacted the overall strength of the storm and to evaluate whether the storm was undergoing a traditional occlusion cycle. Finally, a large-eddy simulation model is used to explore physical changes in a tornado encountering terrain similar to the Mountainburg, Arkansas, tornado near its demise.

1. Introduction

Terrain has been shown to influence tornadic and non-tornadic storms through both empirical (Bosart et al. 2006, Gaffin and Parker 2006, Schneider 2009, Lyza and Knupp 2018, Houser et al. 2020) and modeling studies (Homar et al. 2003, Markowski and Dotzek 2011, Lewellen 2012, Matsangouras et al. 2014, Satrio et al. 2020). Numerous observational studies have been performed across the United States and Europe to describe the effects of terrain influences on tornadogenesis. Bosart et al. (2006) and LaPenta et al. (2005) studied separate tornadoes in the Hudson River Valley, and both came to the same conclusions

Corresponding author address: Matthew E. Anderson, NOAA/Weather Forecast Office Huntsville, Alabama, 320A Sparkman Dr. Huntsville, AL 35805.
E-mail: matt.anderson@noaa.gov

that the river valley helped channel the low-level flow, thereby increasing the storm-relative helicity and theta-e values. Schneider (2009) examined three separate tornadoes across the Tennessee River Valley, concluding that a variety of different topographic configurations may provide the local enhancement of low-level wind shear and instability that are needed for tornadogenesis. Lyza and Knupp (2018) examined 79 tornadoes that occurred from 1992–2016 in the Sand Mountain area of northeastern Alabama. They determined that the channeling of low-level wind and relatively lower Lifted Condensation Levels (LCLs) in the higher terrain may have contributed to the relative maximum of tornadoes in this geographic area. Houser et al. (2020) used rapid-scan radars to compare tornado intensity to ground elevation and surface roughness in five tornadoes across the Great Plains. They concluded that in four of the five cases there was a statistically significant relationship between topographic elevation and tornado intensity, with the strengthening tornado vortex signature observed as the tornado descended in elevation. Topography also can play a role in hindering tornadogenesis or potentially lead to tornado dissipation. Rough terrain can act to block the progression of surface boundaries and inhibit the strength of the low-level jet (Pan et al. 2004). Surface boundaries have been shown to be critical for horizontal vorticity enhancements for low-level mesocyclogenesis (Markowski et al. 1998). Additionally, tilting and stretching of vertical vorticity changes due to ascending (decreasing intensity) or descending (increasing intensity) also may have substantial impacts on the overall tornadic circulation.

Numerous modeling studies have come to the same conclusion that terrain can influence tornadic and non-tornadic storms. Markowski and Dotzek (2011) performed simulations of supercells moving over complex terrain and evaluated how the terrain impacted the near-storm environment. They found higher values of convective inhibition in lower elevations and changes in the low-level wind shear due to topographic modification of the low-level wind field. Lewellen (2012) used a large-eddy simulation (LES) model to simulate tornado-scale circulations in varied terrain and concluded that even small changes in topography can lead to significant changes in tornado strength, path, and structure. Lewellen (2012) also noted that the largest influence from topography was the change in the near-surface inflow to the tornado. Satrio et al. (2020) used an LES to model the impacts of terrain on tornadoes in 29 different simulations grouped into 4 different categories: hill, sinusoidal, valley, and ridge. Satrio et al. (2020) concluded that the introduction of terrain increased the variability of 10-m (32-ft) horizontal and vertical winds, and the variability in wind speeds became more pronounced with an increase in terrain height.

Tornado occurrence over rough terrain is thought to be rare, but there are other factors that may impact the number of reports of tornadoes in areas of rough terrain (e.g., population density, sightlines). Hua and Chavas (2019) examined the relationship between population density and elevation roughness on the probability of tornadogenesis across Arkansas. They concluded that there is a negative effect from elevation roughness on tornadogenesis at fixed population density. Potvin et al. (2019) examined the Storm Prediction Center's tornado database and determined that population density has the most impact on the variance of tornado reports. They also concluded that there are other factors, such as density of storm spotters and chasers and poor sightlines, that may account for the lower number of tornado reports in rough terrain.

This study examines a tornado that developed in northwestern Arkansas on 13 April 2018 in an area of rough terrain. The tornado traveled in a river valley throughout most of its life cycle with a 100–150-m (328–492-ft) ridge on either side before ascending a 200-m (656-ft) hill and dissipating. The synoptic and mesoscale environments are examined to assess the likelihood of tornadogenesis. A detailed topographic analysis is performed to determine what role the terrain might have played in the formation, track, intensity, and demise of the tornado. The tornado's ascension of the ridge is theorized to play a major role in the demise of the tornado. To further investigate this hypothesis, other explanations for the tornado's demise, such as the weakening of the updraft, are addressed by analyzing the Z_{dr} column. The vortex tilt is also examined to determine if the tornado was going through an occlusion cycle. Finally, an LES model is used to model a tornado in a similar topographic environment.

2. Data and methods

Mountainburg is located in the northwestern portion of Arkansas (Fig. 1). Frog Bayou, a tributary of the Arkansas River, runs through the town. The town is located approximately 3 km (1.9 mi) downstream to the southwest of the Fort Smith Lake and Dam. Mountainburg is in a southwest-to-northeast oriented

Figure 1. Tornado path shown in red. *Click image for an external version; this applies to all figures and hereafter.*

valley in the Boston Mountains (Fig. 2) with elevation differences of 100–150 m (328–492 ft) on either side of the valley (Fig. 3). Lake Fort Smith Dam, to the northeast of Mountainburg, represents the northeastern extent of the river valley with roughly a 200-m (656-ft) increase in elevation relative to the valley. Figure 4 provides a visual representation of the 200-m (656 -t) increase in elevation near the Lake Fort Smith Dam.

The National Weather Service (NWS) in Tulsa, Oklahoma, conducted a detailed damage survey of the tornado with many points of impact noted along the path. One of the main goals of this study was to perform a detailed topographic analysis of the tornado path. ArcMap and Google Earth were utilized to accomplish this goal. ArcMap was used to examine a 1-meter (3.3 ft) Digital Elevation Model (DEM) produced by the Arkansas GIS Office. The DEM was used in conjunction with the data points along the storm survey to further assess the elevation associated with the points and the degree of damage. Google Earth was incorporated in the study to provide the reader with a visual assessment of the hill at the end of the tornado's path.

No observational surface data are available in Mountainburg or within the associated river valley. The closest Automated Surface Observing System (ASOS) is located about 35 km (21.7 mi) to the south-southwest of Mountainburg in Fort Smith, Arkansas (Fig. 2). For this study, a sounding and hodograph from the Rapid Refresh Model (RAP; Benjamin et al. 2016) were recreated for Fort Smith at 2100 UTC on 13 April

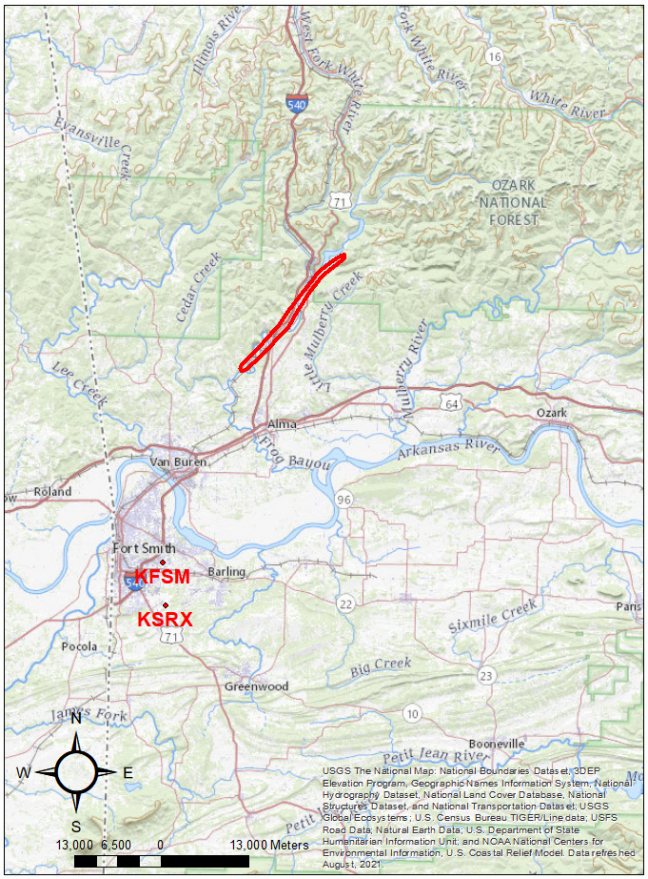

Figure 2. Topographic map surrounding Mountainburg, AR, with tornado track polygon shown in red. KFSM is the Fort Smith, AR, Automated Surface Observing System, and KSRX is the closest radar.

2018. The data were displayed and analyzed using the Rawinsonde Observation Program for Windows (Eosonde Research Services, LLC, 2020). Proximity soundings have limitations and can be unrepresentative at times, especially in areas of complex terrain. The Fort Smith ASOS and proximity sounding were used in this study to substantiate the favorable environment for tornadoes and to assess the predicted storm motion. The nearest Next Generation Weather Radar location is the Weather Surveillance Radar - 1988 Doppler (WSR-88D) in Fort Smith (KSRX), about 43 km (26.7 mi) south-southwest of Mountainburg (Fig. 2).

The tornado formed 30.6 km (19 mi) north-northeast of the KSRX radar. The WSR-88D was operating in Supplemental Adaptive Intra-Volume Low-Level Scan (SAILS) (Daniel et al. 2014) mode throughout the duration of the event. SAILS enables additional low-level (0.5° elevation angle) scans throughout the radar volume scan, which provide 90–120-s temporal resolution updates that allow for more timely data to

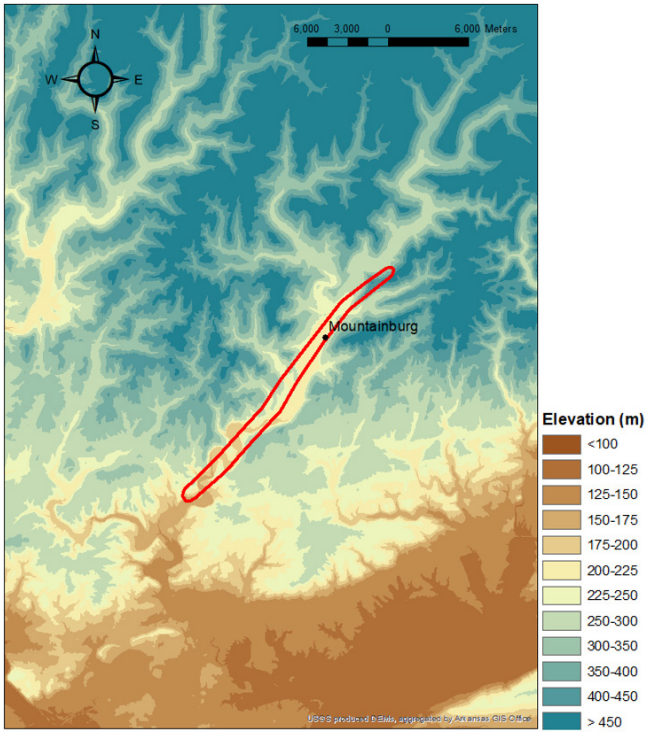

Figure 3. Detailed topographic map of the region around Mountainburg, AR. Elevation data obtained from the Arkansas GIS office's 1 m (3.3 ft) digital elevation model. The path of the tornado is outlined in red.

better correlate velocity changes with the damage survey. KSRX was operating in SAILS-3 during the event, producing three additional 0.5° elevation angles throughout the radar volume scan. Close radar proximity to the storm track and supplemental low-level scans provided ideal radial, vertical, and temporal resolution for analysis of the supercell. Radar data from the Multi-Radar Multi-Sensor System (Smith et al. 2016) were also used in this study to produce a gridded product depicting the maximum values of azimuthal shear (Manross et al. 2008, Karstens et al. 2015, Mahalik et al. 2019).

To support the analyses, several radar parameters were derived from velocity and dual-polarization products. Radar data were examined using the GR2Analyst software to access base parameters (reflectivity and velocity) and dual-polarization variables. The low-level radar rotational velocity [$V_{rot} = (V_{max}–V_{min})/2$] was used to assess the strength of the low-level mesocyclone. To examine hypotheses related to storm-scale evolution, the tilt angle between the tornadic vortex signature (TVS) and the low- and midlevel mesocyclones was analyzed. The TVS center was

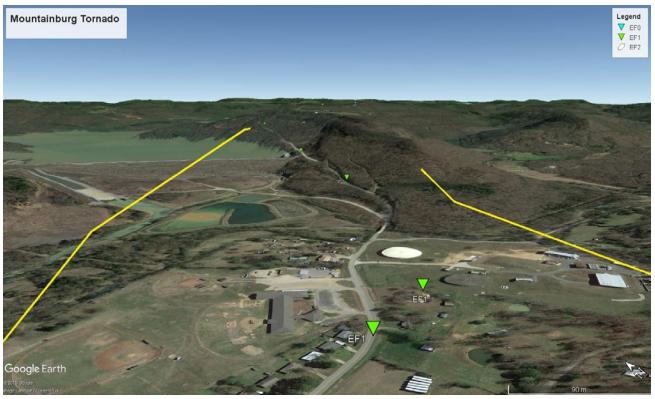

Figure 4. Google Earth Image of tornado polygon in yellow with green icons indicating locations of surveyed tornado damage near the Lake Fort Smith Dam.

identified manually by finding the center point between the maximum and minimum inbound velocities at the 0.5º elevation angle scan. At higher tilts, the velocity maxima commonly were separated by more than 1 km (0.6 mi), resolving mesocyclone-scale motions. For the low-level and midlevel mesocyclone, the elevation angle located closest to 1.5 and 3.0 km (0.9 and 1.9 mi) above ground level (AGL), respectively, was used in the analysis (owing to the change in beam height when selecting a fixed elevation angle). The 0.5º SAILS scan closest in time to the higher elevation angle scan times was used to minimize the impact of advection on vortex tilt, and a linear advection correction was applied based on the mean storm motion.

3. Synoptic and mesoscale overview

A favorable setup for severe storms was present on the evening of 13 April 2018. The synoptic pattern was characterized by an upper-level closed low across Colorado into western Kansas (Fig. 5). An elongated 300 hPa jet of 50–60 m s^{-1} (112–134 mph) stretched from northern Texas into southeastern Nebraska. The location of this jet placed northwestern Arkansas in the favored right-entrance region for mass divergence aloft. Impressive wind velocities were also noted at 500 hPa with a narrow region of winds of more than 40 m s^{-1} (89 mph) (Fig. 5). In the low levels, the low at 850 hPa was located near southeastern Nebraska. Warm air advection was present with southerly flow of 20–25 m s^{-1}(45–56 mph), expanding northward from the northwestern Gulf Coast into the mid-Mississippi River Valley (Fig. 5). The surface low was near the 850-hPa low in southeastern Nebraska, with a cold front extending southward into eastern Kansas and southwestward into the Texas

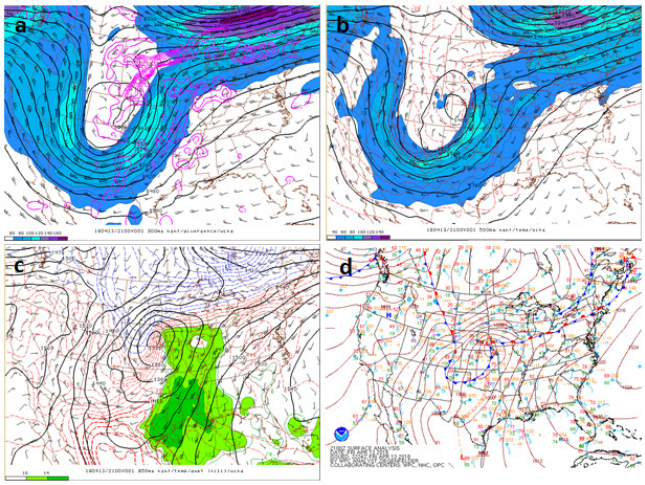

Figure 5. Reanalysis data from 1800 UTC on 13 April 2018 showing (a) 300 hPa isoheights, divergence, and wind barbs; (b) 500 hPa isoheights, temperatures, and winds; (c) 850 hPa isoheights, temperatures, and dewpoints; and (d) winds. Surface analysis from the Weather Prediction Center.

Panhandle (Fig. 5). A dry line extended southward across central Oklahoma and into central Texas. The meteogram from Fort Smith indicated a steady rise in the dewpoint temperatures throughout the afternoon (Fig. 6). Dewpoint temperatures were maximized near the time of the tornado, with values reaching the mid-60's Fahrenheit (~19°C). Southerly to southeasterly winds were observed throughout the afternoon, with values around 3–7 m s^{-1} (7–16 mph) (Fig. 6). Surface pressure also steadily decreased throughout the day as the cold front approached from the west (not shown).

The model sounding depicts a high shear and a low to moderately unstable environment conducive for tornadoes. The 0–1 km, 0–2 km, and 0–3 km storm relative helicity (SRH) values are 312 $m2s^{-2}$, 497 $m2s^{-2}$, and 453 $m2s^{-2}$, respectively (Fig. 7). The Mixed Layer Convective Available Potential Energy was 1016 Jkg^{-1} (Fig. 7). Due to the high dewpoints, the LCL was low and was noted at 539 m (1768 ft) (Fig. 7). The combination of parameters from high low-level shear, moderate instability, and low LCL heights creates a favorable environment for tornadogenesis (Thompson et al. 2003). Overall, the atmosphere on the afternoon and evening of 13 April 2018 was conducive to tornadogenesis across northwestern Arkansas.

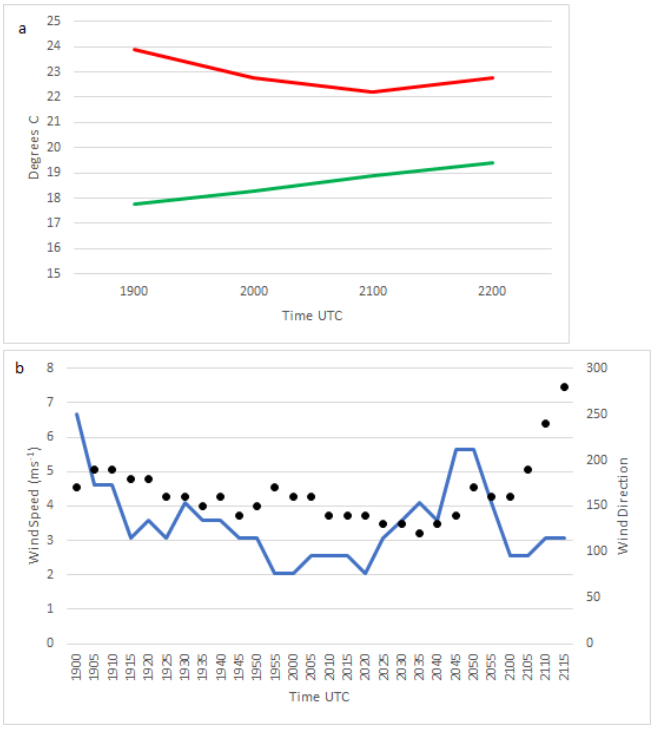

Figure 6. Data from the KFTM ASOS on 13 April 2018 showing (a) temperature (red) and dewpoint (green) in degrees Celsius versus time (UTC) and (b) wind speed in m s^{-1} and wind direction versus time (UTC).

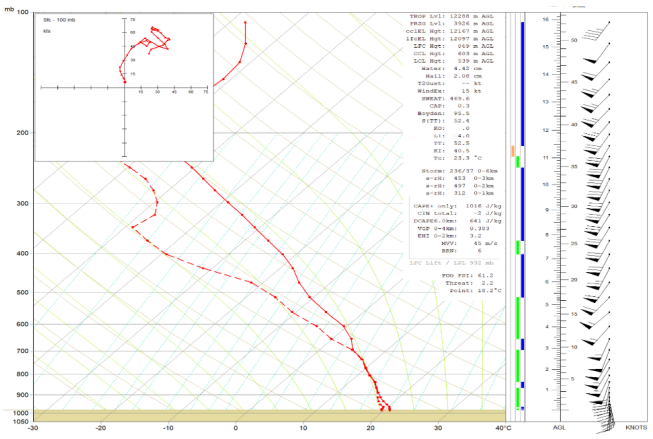

Figure 7. RAP 0-hour forecast sounding from 2100 UTC 13 April 2018 for Fort Smith, AR. Data displayed using the Rawinsonde Observation Program for Windows software.

4. Tornado path and terrain influences

The tornado formed at approximately 2104 UTC at the confluence of the river valley located 12.5 km (7.8 mi) southwest of Mountainburg (Fig. 1). The tornado continued to the northeast on a heading of roughly

40° through Mountainburg (Fig. 3). Throughout its lifecycle, the tornado tracked primarily within the river valley with rises of 100–150 m (3280–492 ft) in elevation on either side. The tornado dissipated at 2119 UTC as it ascended approximately 200 m (656 ft) over the last 1–2 km (0.60–1.2 mi) of its path approaching the Fort Smith Lake Dam (Fig. 4). The damage path ended approximately 6 km (3.7 mi) northeast of Mountainburg, just to the east of Fort Smith Lake. The tornado was rated an EF2 with a total path length of 18.8 km (11.7 mi) with a maximum path width of approximately 900 m (2952 ft) and maximum peak winds of 49–54 m s^{-1} (110–120 mph) (Table 1).

Several factors associated with the rough terrain along the tornado's path may have influenced its development, intensification, and dissipation. The tornado experienced relatively minor upward changes in elevation through most of its life cycle until the last 1–2 km (0.60–1.2 mi) of the path (Fig. 8). The tornado seems to fit into the conceptual model of weakening/dissipating vorticity as the elevation increased by approximately 200 m (656 ft) in the last 1–2 km (0.60–1.2 mi) path of the tornado. At the end of the tornado's track, it ascended a sharp gradient in topography in the area of the Fort Smith Lake and Dam and then dissipated.

The terrain may have also impacted tornadogenesis at the entrance to the river valley. Observations from the Fort Smith ASOS indicated the winds backing to the south-southeast just before the time of tornadogenesis. Geostrophic winds tend to back when increased friction (i.e., rough terrain) is present (Stull 1988), and backing winds lead to higher values of SRH. Using the High-Resolution Rapid Refresh (Lee et al. 2019; NOAA 2021) model, Coleman et al. (2021) examined the effects of heterogeneous surface roughness on the boundary layer in two cases in northeastern Arkansas. They observed an increase in low-level convergence along gradients of surface roughness. Figure 3 depicts how southeasterly flow would experience a rather abrupt change in surface roughness before approaching Boston Mountain in the vicinity of the town of Mountainburg. The low-level winds were not measured in this case but, based on the Coleman et al. (2021) paper, it can be theorized that the surface roughness in the area may have helped enhance low-level convergence. The RAP sounding (Fig. 7) and hodograph (Fig. 9) both depict winds from 170°–180° (southerly flow) around the time of the tornado. It is unlikely that wind-channeling occurred in this scenario, given that the valley orientation was perpendicular to the direction of the low-level winds.

Table 1. Tornado intensity, maximum wind, path length, and maximum path width description. Data obtained from the National Centers for Environmental Information Storm Event database (www.ncdc.noaa.gov/stormevents/eventdetails.jsp?id=747573).

EF Scale	EF2
Max. Estimated Wind Speeds	49–54 m s^{-1}(110–120 mph)
Path Length	18.8 km (11.7 mi)
Max. Path Width	900 m (2952 ft)

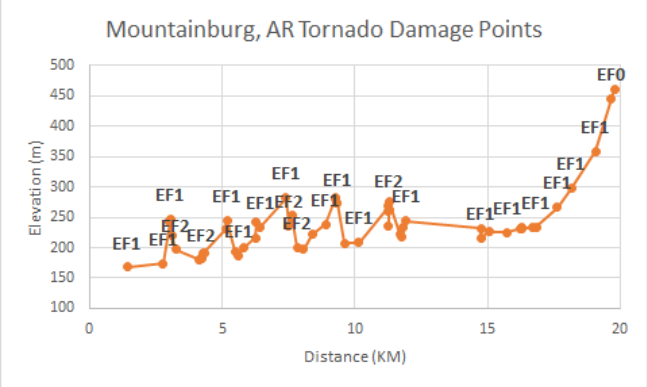

Figure 8. Mountainburg, AR, tornado damage points plotted over the distance versus the elevation of the damage point.

Another important factor to discuss is storm motion. The tornado stayed in the valley throughout the duration of its path. The hodograph indicated a right-motion vector (Bunkers et al. 2000) of 223° at 23 m s^{-1} (51 mph) (Fig. 9). The actual storm motion was 227° at 22 m s^{-1} (49 mph), nearly identical to the right-motion vector. The valley orientation is from southwest to northeast at 40°. The storm motion was likely influenced by the large-scale environment with the near-match of the Bunkers right-motion vector and the valley orientation; however, it is important to explore other theories of how the river valley may have impacted the path and storm motion. As mentioned earlier, the height of the ridge is around 100–150 m (3280–494 ft). This configuration is nearly identical to the valley-modeling configurations performed by Satrio et al. (2020). In their modeling study, they observed that the vortex deflected to the right upon entering the valley. They attributed this in part to suppressed vertical motion due to downsloping flow on the southern side of the storm. Figures 2 and 3 indicate a slight deviation to the right at the beginning of the damage path, supporting the Satrio et al. (2020) findings. Based on the damage points and survey from

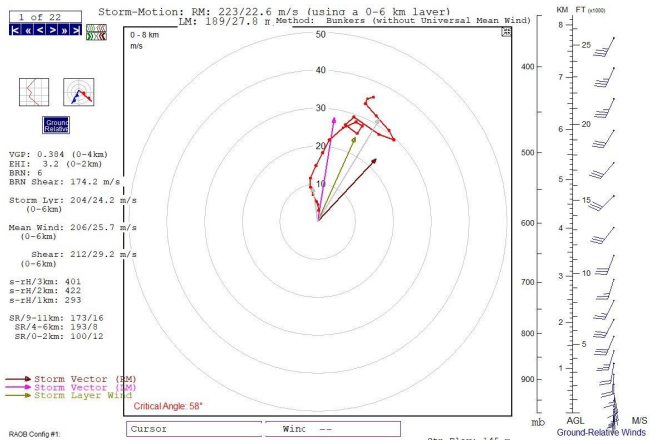

Figure 9. RAP 0-hour forecast hodograph from 2100 UTC 13 April 2018 for Fort Smith, AR. Data displayed using the Rawinsonde Observation Program for Windows software.

Fig. 8, the intensity observed at the damage points shows only minor variations in damage indicators from EF1–EF2 damage. Although it cannot be proved in this study, the downsloping associated with the inflow also may have influenced the intensity of the tornado throughout its time in the river valley by suppressing vertical motion.

5. Radar analysis

The tornado formed 30.6 km (19 mi) north-northeast of the KSRX radar. The height of the radar beam AGL ranged from around 250 m (820 ft) at the beginning of the path to around 750 m (2460 ft) at the end of the path. The 0.5° elevation angle is the lowest scan available and does increase substantially throughout the path. Tornadoes can be quite shallow in some cases, and this data may not be entirely representative of the tornadic circulation, especially near the end of the tornado's path in this case. The 0.5° rotational velocity (V_{rot}) increased from 15 m s^{-1} (29 kt) at 2100 UTC to approximately 24 m s^{-1} (47 kt) at 2104 UTC as the tornado developed (Fig. 10 and Fig. 11). A tornadic debris signature (TDS) (Ryzhkov et al. 2005) became evident during the same volume scan, with the maximum height of the TDS near 2700 m (8858 ft) AGL (not shown). The maximum height of the TDS is consistent with a tornado of EF1–EF2 intensity (Van Den Broeke and Jaurenic 2014). The 0.5° V_{rot} continued to increase and peaked at 32 m s^{-1} (62 kt) at 2109 UTC (Fig. 10 and Fig. 11), at which time the tornado produced EF2 damage. Slow weakening of the 0.5° V_{rot} was observed until 2113 UTC with a V_{rot} of 25 m s^{-1} (49 kt), with a slight increase to 27 m s^{-1} (52

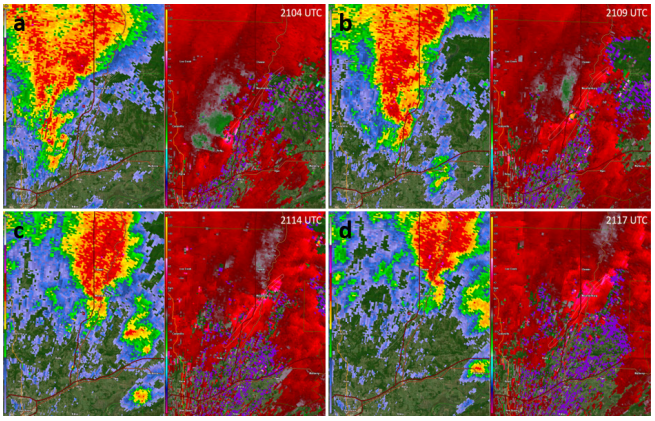

Figure 10. Two-panel depiction of 0.5° reflectivity (left) and velocity (right) at (a) 2104 UTC, (b) 2109 UTC, (c) 2114 UTC, and (d) 2117 UTC. Data reproduced using GR2Analyst.

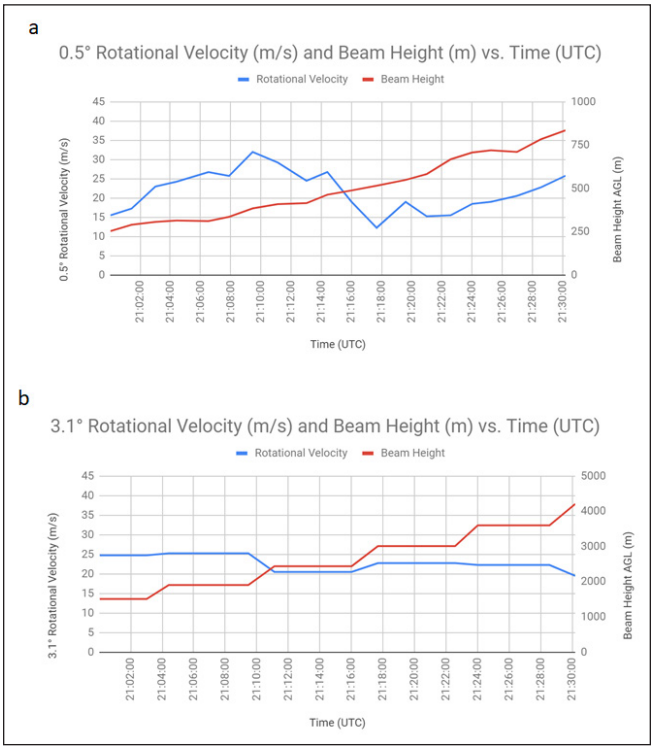

Figure 11. Plot (a) of 0.5° rotational velocity (blue) and beam height (red) versus time (UTC). Plot (b) of 3.1° rotational velocity and beam height versus time.

kt) at 2114 UTC (Fig. 10 and Fig. 11). As the tornado began to encounter elevation increases near Fort Smith Dam, 0.5° V_{rot} decreased rapidly to 12 m s^{-1} (23 kt) between 2114 UTC and 2117 UTC prior to dissipation of the tornado at 47.4 km (29.5 mi) north-northeast of KSRX.

Although 0.5° V_{rot} rapidly decreased and the tornado weakened over the last 2 km (1.2 mi) of the track, the midlevel mesocyclone strength remained nearly constant with V_{rot} of between 21 and 26 m s^{-1} (41 and 51 kt) (Fig. 11) at 2700–3000 m (8858–9842 ft) AGL and no noticeable trends relating to the 0.5° V_{rot}. Although storm movement and distance from the radar will limit analysis of constant elevation, several elevation angles at each scan were able to thoroughly sample the 2700–3000 m (8858–9842 ft) AGL level and provide data for the midlevel mesocyclone magnitude.

Although the radar data and damage survey clearly show that the tornado dissipated while ascending the ridge, additional possibilities for tornado demise should be considered. To determine if the updraft was weakening or the supercell's updraft was occluding, the differential reflectivity (Z_{dr}) column (Bringi et al. 1991; Loney et al. 2002; Kumjian et al. 2014) and vortex tilt were examined. The height and aerial extent of the Z_{dr} column has been found to be a good proxy for evaluating the strength of the updraft (Scharfenberg et al. 2005, Picca et al. 2010, Kumjian et al. 2014). A slightly modified Z_{dr} column algorithm described in Snyder et al. (2015) is used to quantify the height of the Z_{dr} column. The 0000 UTC RAP sounding from Fort Smith, Arkansas, was used to determine the height of the environmental freezing level. Data were interpolated to a 250x250x250-m (820x820x820 ft) grid, similar to Snyder et al. (2015). Using the interpolated data, a Z_{dr} column was identified anywhere continuous vertical grid points were observed with Z_{dr} greater than 1 dB above the environmental freezing level determined from the RAP sounding. A time series of Z_{dr} column height from the algorithm output is shown in Fig. 12. The mean Z_{dr} column height is the mean value over a 5-km (3.1 mi) radius surrounding the manually identified mesocyclone location, whereas the maximum is the largest value seen in the 5-km (3.1 mi) radius. Around the time of dissipation, the mean and maximum Z_{dr} column height were both greater than prior to and just after tornadogenesis. Decreasing height of the Z_{dr} column may indicate updraft weakening and lead to tornado demise (Houser et al. 2015). Van Den Broeke (2017) showed clear distinctions between the height of the Z_{dr} column above the melting level in distinguishing between weak and strong tornadoes. The Z_{dr} column height remained unchanged around the time of tornado's demise, suggesting that the updraft remained intense leading up to and after tornado dissipation. Thus, tornado decay does not appear to be the result of a weakening storm-scale updraft.

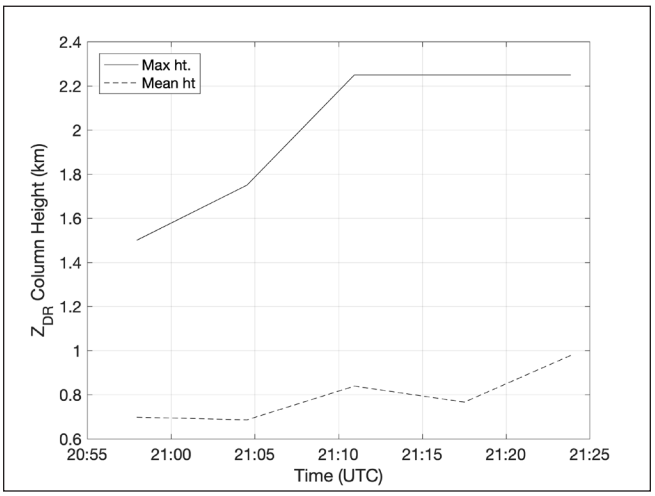

Figure 12. Maximum and mean Z_{dr} column height (km) from KSRX between 2057 and 2124 UTC. The storm maintained a robust updraft leading up to and after tornado dissipation between 2114 and 2117 UTC.

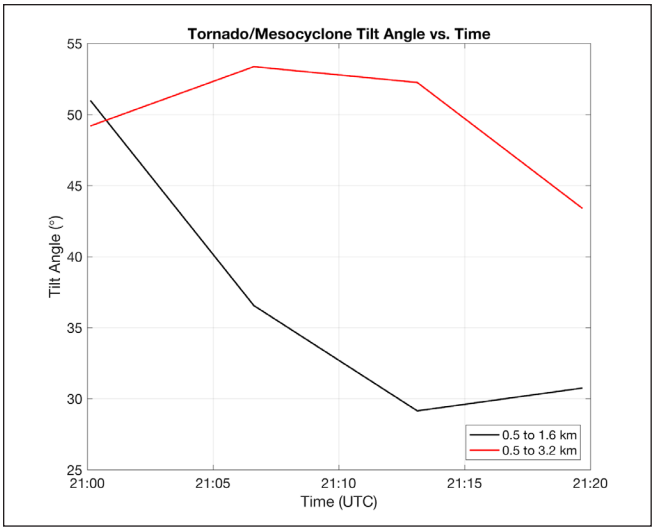

Figure 13. Tilt angle of the low-level circulation between 0.5 and 1.6 km (0.3 and 1 mi) (black line) and 0.5 and 3.2 km (0.3 and 2 mi) (red line). The low-level mesocyclone's tilt angle decreased leading to tornado dissipation around 2114–2117 UTC.

Vortex tilt was computed from the lowest elevation angle scan and altitude representative of the low- and midlevel mesocyclone using manually identified vortex center locations. The tilt analysis is shown in Fig. 13. Tornado and mesocyclone tilt at low levels [between 0.5 and 1.6 km layer (0.3 and 1 mi layer)] decreased from more than 50º to less than 29º just prior to tornado dissipation. The tilt between the tornado and midlevel mesocyclone was 49º around tornadogenesis and 53º

just prior to tornado dissipation, which are fairly similar values. Based on the observations of vortex tilt, it did not appear that the tornado and low-level mesocyclone were becoming substantially more tilted at the time of tornado dissipation as commonly occurs during the occlusion process of tornadoes (French et al. 2014; Griffin et al. 2019). There are also no indications of rear-flank downdraft surge or left-of-storm motion by the tornado, which can be signs of occlusion as well. French et al. (2014) and Griffin et al. (2019) observed that an increase in vortex tilt can lead to tornado dissipation as the low-level circulation becomes more westerly and removed from the parent storm as the tornado occludes. Combined, these two analyses support the assertion the supercell was not undergoing an occlusion cycle and that other factors influenced the low-level V_{rot} and tornado intensity and instigated tornado dissipation.

6. Model simulations

Because close-range observations over complex terrain are difficult to obtain, high-resolution numerical simulations from an LES model (Maruyama 2011; Bodine et al. 2016) are used to explore physical changes in a tornado encountering terrain similar to the Mountainburg tornado near its demise. The tornado vortex is developed within the LES model by imposing a converging, swirling flow along the side of the model domain. A central updraft is imposed at the top of the domain with an embedded central downdraft. The LES model uses an immersed boundary method (Saiki and Birigen, 1996) to represent the terrain such that arbitrary topography can be represented. For details on the suite of simulations over complex terrain and the methods, the reader is referred to Satrio et al. (2020).

The simulated idealized tornado is initially developed over flat terrain, and simulations are run until the vortex reaches a steady state. Prior to encountering terrain, the tornado is a multiple vortex tornado with a radius of maximum wind of approximately 100 m. In the absence of terrain, the simulation produces a 95th percentile horizontal wind of 55.5 m s^{-1} (124 mph) along its track but contains small areas where winds exceed 70 m s^{-1} (157 mph). Owing to the coarse resolution of the NEXRAD data, it is not possible to create a simulation that exactly matches the observed tornado's winds. However, the numerical simulation does reproduce some tornado structure seen in video observations from the Mountainburg tornado (e.g., subvortices). The caveat is that different types of tornado flows may have different responses to complex terrain, but this detailed sensitivity analysis is beyond the scope of this paper.

Three different simulations were completed to examine the effects of a tornado encountering a ridge after residing inside a valley and the tornado crossing the ridge at a 45º angle (i.e., to the northeast). Maximum horizontal wind speeds at 10 m (32 ft) AGL along the track are shown in Fig. 14 for a 50-m (164 ft), 100-m (328 ft), and 200-m (656 ft) ridge (the latter corresponding to the Mountainburg case). First, the tornado bounded by the taller ridge has slightly stronger winds prior to ascending the ridge compared to the other two simulations, consistent with other simulations shown in Satrio et al. (2020). Upon ascending the 50- and 100-m (164 and 328-ft) ridge, the tornado intensifies. In contrast, the 200-m (656-ft) ridge has a disruptive effect, and the tornado weakens upon encountering the steep slope and remains weaker and more disorganized at the top of the ridge. This is consistent with the radar observations of a weakening vortex after ascending the 200-m (656-ft) ridge as well as a broader and more disorganized circulation. Satrio et al. (2020) [using a hill terrain set of 25 m (82 ft), 50 m (164 ft), and 100 m (328 ft] noted that terrain enhanced the tornado's winds for small variations in terrain (e.g., <100 m or <328 ft) but was disruptive for larger changes in elevation. Satrio et al. (2020) did not model a hill of the magnitude in this case (200 m or 656 ft), but Fig. 14 clearly indicates the disruptive nature with increasing elevation in the modeled tornado.

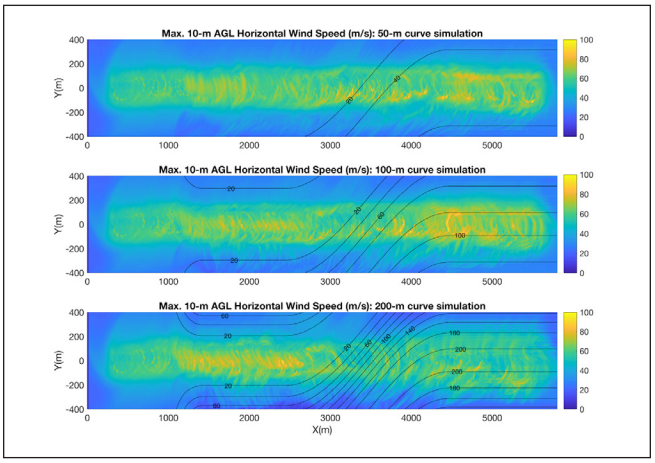

Figure 14. Simulations of a tornado entering a valley and then ascending a ridge at an angle where the valley curves 45° to its left. The maximum heights of the ridge are set to 50, 100, and 200 m (164, 328, and 656 ft) (top, middle, bottom).

A few caveats are noted for the interpretation of these simulations for terrain effects. First, the model does not have a parent thunderstorm (owing to the high-resolution required for such simulations), and thus the effects of terrain on the parent storm are unknown and not modeled. It is possible that the low-level mesocyclone's updraft and available angular momentum also diminished and contributed to the weakening of the tornado. In contrast, the present simulations have updraft velocities and angular momentum specified as constant values. Thus, the simulated tornado does not fully dissipate, whereas the actual tornado did dissipate. Nonetheless, the weakening of the tornado upon ascending the ridge is consistent with the observed trends in Doppler velocity, and thus physical insight can be attained.

7. Conclusions

An empirical and modeling study was conducted to examine the effects of terrain on the formation and dissipation of the Mountainburg, Arkansas, tornado. The empirical evidence through radar data, model soundings, terrain orientation, and surface observations suggests that the terrain may have influenced the tornado's formation but had a more definitive role in the tornado's dissipation. The midlevel V_{rot}, Z_{dr} column, and vortex tilt all suggest that external factors contributed to the tornado's demise other than a traditional occlusion cycle (e.g., Lemon and Doswell, 1979). The tornado may very well have dissipated regardless of the terrain, but the examination of the high-resolution radar data, Zdr column, and vortex tilt all suggest there was an external factor by pinpointing the weakening of the tornado at the time of the elevation rise. The Bunkers right-motion vector suggests that the valley's orientation and storm motion were nearly identical, and the storm motion was most likely influenced by the large-scale environment rather than channeling effects associated with the terrain. Although this study was not able to assess exactly what impact the terrain had on the vortex that made it dissipate, the conclusion of this study is that the abrupt 200-m (656-ft) ascension of a hill near the Fort Smith Lake and Dam was the external factor that contributed to the weakening of the tornado. To further illustrate this point, the LES model was used to simulate a tornado and how it interacted with similar terrain. The simulation that was most similar (200 m or 656 ft) to the elevation rise of the Mountainburg tornado produced similar results, with the tornado weakening as it ascended a rather abrupt rise of 200 m (656 ft). The model does not have a parent thunderstorm; therefore, it is unknown if the midlevel mesocyclone would evolve in a similar situation as the Mountainburg tornado. The theory that the tornado was undergoing an occlusion cycle was addressed by examining the midlevel Vrot, Z_{dr} column, and vortex tilt. Overall, the empirical and model data support the hypothesis that the tornado dissipation was at least in part initiated by the terrain.

8. Future work

A few cases of tornadoes and terrain were noted previously in this paper, but more cases of tornadoes in rough terrain would be beneficial. Overall, cases of tornadoes in rough terrain are relatively rare compared to tornadoes that occur in terrain with minor changes in elevation. Extensive damage surveys of these tornadoes also would be helpful. This case involved a thorough survey by the NWS in Tulsa, Oklahoma, throughout the lifecycle of the tornado. In addition, the observational techniques introduced here to examine storm-scale factors can aid in identifying storm-scale processes that may affect tornado evolution in addition to terrain, improving upon correlation-based analyses done to date. Along with increased cases, more robust modeling would be beneficial in studying tornadoes and terrain interaction. The LES model has several limitations as noted previously in the paper. More sophisticated high-resolution modeling with terrain could add to the thesis regarding how tornadoes evolve over complex terrain. Orf (2019) modeled a tornado with more than a quarter of a trillion grid volumes. This extensive modeling was outside of the scope of this study but would provide useful information to examine how terrain may have had an impact in tornadogenesis and the demise of the tornado in a similar case.

Acknowledgments. M. Anderson, J. Buckles, and D. Schneider would like to thank David Hotz, the Science and Operations Officer at the NWS in Morristown, TN, for his guidance and review of this manuscript. D. Bodine and A. Reinhart are supported by grants VORTEX-SE NA17OAR4590201, NA17OAR4590202, and NA19OAR4590216. In addition, D. Bodine is supported by NSF AGS-1823478 and AGS-2114817. We thank Professor Takanori Uchida at Kyushu University for providing the RIAM-COMPACT software and allowing its use for this research project. We also would

like to acknowledge three anonymous reviewers, whose comments greatly improved the manuscript.

REFERENCES

Benjamin, S. G., and Coauthors, 2016: A North American hourly assimilation and model forecast cycle: The Rapid Refresh. *Mon. Wea. Rev.*, **144**, 1669–1694, CrossRef.

Bodine, D. J., T. Maruyama, R. D. Palmer, C. J. Fulton, H. B. Bluestein, and D. C. Lewellen, 2016: Sensitivity of tornado dynamics to soil debris loading. *J. Atmos. Sci.*, **73**, 2783–2801, CrossRef.

Bosart, L. F., A. Seimon, K. D. LaPenta, and M. J. Dickinson, 2006: Supercell tornadogenesis over complex terrain: The Great Barrington, Massachusetts, tornado on 29 May 1995. *Wea. Forecasting*, **21**, 897–922, CrossRef.

Bringi, V. N., D. A. Burrows, and S. M Menon, 1991: Multiparameter radar and aircraft study of raindrop spectral evolution in warm-based clouds. *J. Appl. Meteor. Climatol.*, **30**, 853–880, CrossRef.

Bunkers, M. J., B. A. Klimowski, J. W. Zeitler, R. L. Thompson, and M. L. Weisman, 2000: Predicting supercell motion using a new hodograph technique. *Wea. Forecasting*, **15**, 61–79, CrossRef.

Coleman, T. A., K. R. Knupp, and P. T. Pangle, 2021: The effects of heterogeneous surface roughness on boundary-layer kinematics and wind shear. *Electronic J. Severe Storms Meteor.*, **16**, 1. [Available online at ejssm.com/ojs/index.php/site/article/view/80/78.]

Daniel, A. E., J. N. Chrisman, S. D. Smith, and M. W. Miller, 2014: New WSR-88D operational techniques: Responding to recent weather events. Preprints, *30th Conf. on Environmental Information Processing Technologies*, Atlanta, GA, Amer. Meteor. Soc., 5.2. [Available online at ams.confex.com/ams/94Annual/webprogram/Paper241216.html.]

Eosonde Research Services, LLC, 2020: RAOB: The complete RAwinsonde OBservation program; User guide & technical manual, Version 6.9. Eosonde Research Services, LLC, The Villages, FL, 207 pp. [Available online at www.raob.com/pdf/RAOB69UserManual.pdf.]

French, M. M., H. B. Bluestein, I. PopStefanija, C. A. Baldi, and R. T. Bluth, 2014: Mobile, phased-array, Doppler radar observations of tornadoes at X band. *Mon. Wea. Rev.*, **142**, 1010–1036, CrossRef.

Gaffin, D. M., and S. S. Parker, 2006: A climatology of synoptic conditions associated with significant tornadoes across the southern Appalachian region. *Wea. Forecasting*, **21**, 735–751, CrossRef.

Griffin, C. B., D. J. Bodine, J. M. Kurdzo, A. Mahre, and R. D. Palmer, 2019: High-temporal resolution observations of the 27 May 2015 Canadian, Texas, tornado using the atmospheric imaging radar. *Mon. Wea. Rev.*, **147**, 873–891, CrossRef.

Homar, V., M. Gayà, R. Romero, C. Ramis, and S. Alonso, 2003: Tornadoes over complex terrain: An analysis of the 28th August 1999 tornadic event in eastern Spain. *Atmos. Res.*, 67–68, 301–317, CrossRef.

Houser, J. B., N. McGinnis, K. M. Butler, H. B. Bluestein, J. C. Snyder, and M. M. French, 2020: Statistical and empirical relationships between tornado intensity and both topography and land cover using rapid-scan radar observation and GIS. *Mon. Wea. Rev.*, **148**, 4313–4338, CrossRef.

Houser, J. L., H. B. Bluestein, and J. C. Snyder, 2015: Rapid-scan, polarimetric, Doppler radar observations of tornadogenesis and tornado dissipation in a tornadic supercell: The "El Reno, Oklahoma" storm of 24 May 2011. *Mon. Wea. Rev.*, **143**, 2685–2710, CrossRef.

Hua, Z., and D. R. Chavas, 2019: The empirical dependence of tornadogenesis on elevation roughness: Historical record analysis using Bayes's Law in Arkansas. *J. Appl. Meteor. Climatol.*, **58**, 401–411, CrossRef.

Karstens, C. D., and Coauthors, 2015: Evaluation of a probabilistic forecasting methodology for severe convective weather in the 2014 Hazardous Weather Testbed. *Wea. Forecasting*, **30**, 1551–1570, CrossRef.

Kumjian, M. R., A. P. Khain, N. Benmoshe, E. Ilotoviz, A. V. Ryzhkov, and V. T. J. Phillips, 2014: The anatomy and physics of Zdr columns: Investigating a polarimetric radar signature with a spectral bin microphysical model. *J. Appl. Meteor. Climatol.*, **53**, 1820–1843, CrossRef.

LaPenta, K. D., L. F. Bosart, T. J. Galarneau Jr., and M. J. Dickinson, 2005: A multiscale examination of the 31 May 1998 Mechanicville, New York, Tornado. *Wea. Forecasting*, **20**, 494–516, CrossRef.

Lee, T. R., M. Buban, D. D. Turner, T. P. Meyers, and C. B. Baker, 2019: Evaluation of the High-Resolution Rapid Refresh (HRRR) model using near-surface meteorological and flux observations from northern Alabama. *Wea. Forecasting*, **34**, 635–663, CrossRef.

Lemon, L. R., and C. A. Doswell III, 1979: Severe thunderstorm evolution and mesocyclone structure as related to tornadogenesis. *Mon. Wea. Rev.*, **107**, 1184–1197, CrossRef.

Lewellen, D. C., 2012: Effects of topography on tornado dynamics: A simulation study. *26th Conf. on Severe Local Storms*, Nashville, TN, Amer. Meteor. Soc., 4B.1. [Available online at ams.confex.com/ams/26SLS/webprogram/Paper211460.html.]

Loney, M. L., D. S. Zrnić, J. M. Straka, and A. V. Ryzhkov, 2002: Enhanced polarimetric radar signatures above the melting level in a supercell storm. *J. Appl. Meteor. Climatol.*, **41**, 1179–1194, CrossRef.

Lyza, A. W., and K. R. Knupp, 2018: A background investigation of tornado activity across the southern Cumberland Plateau terrain system of northeastern Alabama. *Mon. Wea. Rev*., **146**, 4261–4278, CrossRef.

Mahalik, M. C., B. R. Smith, K. L. Elmore, D. M. Kingfield, K. L. Ortega, and T. M. Smith, 2019: Estimates of gradients in radar moments using a linear least squares derivative technique. *Wea. Forecasting*, **34**, 415–434, CrossRef.

Manross, K. L., T. M. Smith, J. T. Ferree, and G. J. Stumpf, 2008: An on-demand user interface for requesting multi-radar, multi-sensor time accumulated products to support severe weather verification. *24th Conf. on Interactive Information Processing Systems*, New Orleans, LA, Amer. Meteor. Soc., P2.13. [Available online at ams.confex.com/ams/pdfpapers/134621.pdf.]

Markowski, P. M., E. N. Rasmussen, and J. M. Straka, 1998: The occurrence of tornadoes in supercells interacting with boundaries during VORTEX-95. *Wea. Forecasting*, **13**, 852–859, CrossRef.

____, and N. Dotzek, 2011: A numerical study of the effects of orography on supercells. *Atmos. Res*., **100**, 457–478, CrossRef.

Maruyama, T., 2011: Simulation of flying debris using a numerically generated tornado-like vortex. *J. Wind Eng. Ind. Aerodyn*., **99**, 249–256, CrossRef.

Matsangouras, I. T., I. Pytharoulis, and P. T. Nastos, 2014: Numerical modeling and analysis of the effect of complex Greek topography on tornadogenesis. *Nat. Hazards Earth Syst. Sci*.,**14**, 1905–1919, CrossRef.

Orf, L., 2019: A violently tornadic supercell thunderstorm simulation spanning a quarter-trillion grid volumes: Computational challenges, I/O framework, and visualizations of tornadogenesis. *Atmosphere*, **10**, 578, CrossRef.

Pan, Z., M. Segal, and R. W. Arritt, 2004: Role of topography in forcing low-level jets in the central United States during the 1993 flood-altered terrain simulations. *Mon. Wea. Rev*., **132**, 396–403, CrossRef.

Picca, J. C., M. R. Kumjian, and A. V. Ryzhkov, 2010: Z_{dr} columns as a predictive tool for hail growth and storm evolution. *25th Conf. on Severe Local Storms*, Denver, CO, Amer. Meteor. Soc., Extended Abstracts, 11.3. [Available online at ams.confex.com/ams/25SLS/techprogram/paper_175750.htm.]

Potvin, C. K., C. Broyles, P. S. Skinner, H. E. Brooks, and E. Rasmussen, 2019: A Bayesian hierarchical modeling framework for correcting reporting bias in the U.S. tornado database. *Wea. Forecasting*, **34**, 15–30, CrossRef.

Ryzhkov, A. V., T. J. Schuur, D. W. Burgess, and D. S. Zrnic, 2005: Polarimetric tornado detection. *J. Appl. Meteor. Climatol*., **44**, 557–570, CrossRef.

Saiki, E. M., and S. Biringen, 1996: Numerical simulation of a cylinder in uniform flow: Application of a virtual boundary method. *J. Comput. Phys*., **123**, 450–465, CrossRef.

Satrio, M. A., D. J. Bodine, A. E. Reinhart, T. Maruyama, and F. T. Lombardo, 2020: Understanding how complex terrain impacts tornado dynamics using a suite of high-resolution numerical simulations. *J. Atmos. Sci*., **77**, 3277–3300, CrossRef.

Scharfenberg, K. A., et al., 2005: The joint polarization experiment: Polarimetric radar in forecasting and warning decision making. *Wea. Forecasting*, **20**, 775–788, CrossRef.

Schneider, D. G., 2009: The impact of terrain on three cases of tornadogenesis in the Great Tennessee Valley. *Electron. J. Oper. Meteor*., EJ11, CrossRef.

Smith, T. M., and Coauthors, 2016: Multi-Radar Multi-Sensor (MRMS) severe weather and aviation products: Initial operating capabilities. *Bull. Amer. Meteor. Soc*., **97**, 1617–1630, CrossRef.

Snyder, J. C., A. V. Ryzhkov, M. R. Kumjian, A. P. Khain, and J. Picca, 2015: A Zdr column detection algorithm to examine convective storm updrafts. *Wea. Forecasting*, **30**, 1819–1844, CrossRef.

Stull, R. B., 1988: *An Introduction to Boundary Layer Meteorology*. Kluwer Academic Publishers, 684 pp.

Thompson, R. L., R. Edwards, J. A. Hart, K. L. Elmore, and P. Markowski, 2003: Close proximity soundings within supercell environments obtained from the Rapid Update Cycle. *Wea. Forecasting*, **18**, 1243–1261, CrossRef.

Van Den Broeke, M. S., and S. T. Jaurenic, 2014: Spatial and temporal characteristics of polarimetric tornadic debris signatures. *J. Appl. Meteor. Climatol*. **53**, 2217–2231, CrossRef.

____, 2017: Polarimetric radar metrics related to tornado life cycles and intensity in supercell storms. *Mon. Wea. Rev*., **145**, 3671–3686, CrossRef.